

Lattice Dynamics of Ultrathin FeSe Films on SrTiO₃

Shuyuan Zhang,^{1,2} Jiaqi Guan,^{1,2} Yan Wang,³ Tom Berlijn,^{4,5} Steve Johnston,³ Xun Jia,^{1,2}
Bing Liu,^{1,2} Qing Zhu,^{1,2} Qichang An,^{1,2} Siwei Xue,^{1,2} Yanwei Cao,¹ Fang Yang,¹
Weihua Wang,¹ Jiandi Zhang,⁶ E. W. Plummer,⁶ Xuetao Zhu,^{1,2,*} and Jiandong Guo^{1,2,7,†}

¹Beijing National Laboratory for Condensed Matter Physics and Institute of Physics, Chinese Academy of Sciences, Beijing 100190, China

²School of Physical Sciences, University of Chinese Academy of Sciences, Beijing 100049, China

³Department of Physics and Astronomy, University of Tennessee, Knoxville, Tennessee 37996, USA

⁴Center for Nanophase Materials Sciences, Oak Ridge National Laboratory, Oak Ridge, Tennessee 37831, USA

⁵Computational Sciences and Engineering Division, Oak Ridge National Laboratory, Oak Ridge, Tennessee 37831, USA

⁶Department of Physics and Astronomy, Louisiana State University, Baton Rouge, Louisiana 70808, USA

⁷Collaborative Innovation Center of Quantum Matter, Beijing 100871, China

(Dated: January 8, 2018)

Charge transfer and electron-phonon coupling (EPC) are proposed to be two important constituents associated with enhanced superconductivity in the single unit cell FeSe films on oxide surfaces. Using high-resolution electron energy loss spectroscopy combined with first-principles calculations, we have explored the lattice dynamics of ultrathin FeSe films grown on SrTiO₃. We show that, despite the significant effect from the substrate on the electronic structure and superconductivity of the system, the FeSe phonons in the films are unaffected. The energy dispersion and linewidth associated with the Fe- and Se-derived vibrational modes are thickness- and temperature-independent. Theoretical calculations indicate the crucial role of antiferromagnetic correlation in FeSe to reproduce the experimental phonon dispersion. Importantly, the only detectable change due to the growth of FeSe films is the broadening of the Fuchs-Kliwer (F-K) phonons associated with the lattice vibrations of SrTiO₃(001) substrate. If EPC plays any role in the enhancement of film superconductivity, it must be the interfacial coupling between the electrons in FeSe film and the F-K phonons from substrate rather than the phonons of FeSe.

I. INTRODUCTION

The superconducting transition temperature (T_C) for monolayer FeSe films, with the thickness of one unit cell (uc), on SrTiO₃(001) substrate (1uc-FeSe/STO)^{1,2} is significantly enhanced to $\sim 60 - 70$ K³⁻⁶ (even probably up to 109 K⁷) compared to bulk FeSe (8 K)⁸. This discovery serves as a prototypical example of interfacial T_C enhancement, which has drawn the attention of the community⁹⁻¹³. Although the mechanism of the interfacial T_C enhancement is not fully understood, electron doping from STO substrates due to the oxygen vacancies⁶ or band bending¹⁴ at interface is widely believed to be an indispensable ingredient^{15,16}. On the other hand, in the systems such as the intercalated (Li,Fe)OHFeSe^{17,18}, and thick FeSe films/flakes with alkali metal adatoms¹⁹⁻²² or ionic liquid gating²³⁻²⁵, where the electron density of the FeSe layer can reach a value as high as that in 1uc-FeSe/STO, the T_C is enhanced only up to ~ 40 K. Thus, electron doping is not the only contributor to the increased T_C . There must be other interfacial effects involved to give rise to the extra ~ 20 K enhancement in 1uc-FeSe/STO.

From the structural point of view, the tensile strain induced by lattice mismatch^{1,6,26} leads to the formation of strain strips¹. The specific interfacial structure with a double-TiO_x termination has been observed by scanning transmission electron microscopy^{27,28}, and thus the vibration of Ti-O bond might be crucial. Similar T_C enhancement behavior has also been discovered in 1uc-FeSe grown on various oxide substrates with Ti-O bonds such as BaTiO₃(001)²⁹, SrTiO₃(110)^{30,31}, anatase TiO₂(001)³², and rutile TiO₂(001)³³, all with different lattice constants and crystal orientations. These results suggest that it is essential

to understand the interfacial lattice dynamics.

From the dynamical point of view, phonons have been studied to elucidate the possible contribution to the interfacial T_C enhancement. Some studies have proposed that Fe- and Se-derived phonons (FeSe phonons) could participate in the interfacial T_C enhancement, which is supported by electron scattering with FeSe phonons in inelastic electron tunneling spectroscopy measurements³⁴. Electron-phonon coupling (EPC) of FeSe phonons is also addressed by ab initio calculations³⁵⁻³⁷. On the other hand, several investigations have shown that phonons from STO substrate can strongly interact with the electrons in the FeSe film as evidenced by the observations of FeSe band replica^{5,9,38} in angle resolved photoemission spectroscopy (ARPES) measurements and the penetration of the STO Fuchs-Kliwer (F-K) phonons into FeSe film in high-resolution electron energy loss spectroscopy (HREELS) measurements³⁹. However, none of the above studies provide the lattice dynamical information of FeSe films, such as the phonon energy and linewidth as a function of wavevector, which can be used to understand the EPC related to superconductivity enhancement.

If phonons are involved in the interfacial enhancement of T_C , several essential questions arise: Which phonons provide the major contribution, the FeSe phonons in the thin film or the STO phonons in the substrate? As the dipole field generated by the STO phonons can penetrate into the thin FeSe film³⁹, are the FeSe phonons affected by the STO lattice and its dynamics? In this paper, we address these questions by measuring the lattice dynamics using HREELS. We demonstrate that although the electronic structure and superconducting behavior vary in films with different thicknesses, the lattice dynamics (phonon spectra and Debye temperature) of Fe-

and Se-derived phonons remain unchanged (from 1uc to 10uc thickness). Thus FeSe phonons are not the essential component in the enhanced interfacial superconductivity. Additionally, the first-principles calculation shows that the antiferromagnetic (AFM) correlation in FeSe is indispensable to quantitatively reproduce the experimental phonon dispersions in the ultrathin FeSe films, suggesting that the magnetic correlation or spin fluctuation is critical not only in FeSe bulk^{40,41} but also in 1uc-FeSe films. In contrast, surface F-K phonon modes of the STO(001) substrate are strongly temperature-dependent, and clearly broaden after the growth of FeSe films. These results indicate that the penetrating substrate F-K phonon field, interacting with electrons therein, provides additional glue for the existing electron pairing of FeSe.

II. EXPERIMENTS AND METHODS

Lattice dynamics including phonon spectra^{42–45} and Debye temperature^{45–49}, can be obtained using techniques such as inelastic x-ray scattering⁴², Raman scattering⁴³, inelastic neutron scattering⁴⁴, nuclear inelastic scattering⁴⁵, specific heat^{46,47}, elastic constant^{48,49}, *etc.* These techniques, however, only measure the bulk properties of materials. Substrate effects on an individual phonon branch of ultrathin films, such as FeSe, can only be measured utilizing surface-sensitive techniques such as HREELS or inelastic helium atom scattering⁵⁰. Due to the limitation of the polycrystal nature of FeSe bulk in pervious studies^{45,51}, the phonon dispersions of FeSe have not been obtained. Here, the combination of a momentum-resolved surface-sensitive technique (HREELS) and the growth of high-quality single crystalline FeSe films allows for the first observation of the phonon dispersions.

A. Preparation of Oxide Substrates

In this study, HREELS measurements were performed on various different samples, including single crystalline oxides, oxide films, and ultrathin single crystalline FeSe films grown on single crystalline oxides. The samples and the preparation methods are summarized in Table.I. The Nb-doped (0.5%) SrTiO₃ substrates are annealed at 600°C for 12 h and then at 950°C for 1 h in ultra-high vacuum (UHV) condition, which is labeled as "treated STO" in the paper and is used as the substrate of FeSe films. The treated STO samples are covered by thick amorphous selenium layer at room temperature, and annealed at 600 °C to remove the Se capping layer before HREELS measurements. To compare with treated STO, another Nb-doped (0.5%) SrTiO₃ substrate is etched by HF and annealed at 600 °C for 12 h before EELS measurement, which is labeled as "clean STO" in this paper. 40uc SrTiO₃ films without Nb doping are grown by pulsed laser deposition (PLD) at 600°C in UHV condition and labeled as "clean STO (w/o Nb)". 40uc BaTiO₃ films are grown by PLD at 670°C in UHV condition. Both clean STO (w/o Nb) and BaTiO₃ films are annealed at 600 °C for 12 h before EELS measurement. TiO₂(110) substrates are annealed at 600°C for 12 h and then

at 900°C for 1 min in UHV condition. The SrTiO₃(110) substrates with two different surface reconstructions, 2×8 and 4×1 superlattices respect to the lattice of STO(110) surface, are prepared using the method in Ref.52.

B. Growth of FeSe films

High-quality single crystalline FeSe films were grown by co-depositing high-purity Fe (99.99%) and Se (99.99+%) with a flux ratio of $\sim 1 : 20$ onto the treated STO held at 400 °C. The as-prepared samples were post-annealed at 470 °C for 5 h in UHV to make the first layer FeSe superconducting. The *in-situ* scanning tunneling microscopy (STM) measurements were performed to confirm the sample quality [Fig. 1 (a)]. 1uc, 3uc and 10uc-FeSe/STO samples were capped with thick amorphous Se layer at 300 K and transferred to our two-dimensional (2D) HREELS system⁵³. The Se capping layer was removed by *in-situ* annealing at 450 °C for 1uc-FeSe/STO and 400 °C for 3uc and 10uc-FeSe/STO. ARPES measurements were performed for 1uc-FeSe/STO to determine the superconducting gap and the superconducting transition temperature $T_C \sim 65$ K. The Debye temperature measurements were performed using low energy electron diffraction (LEED) on 1uc and 10uc-FeSe/STO samples.

C. ARPES Measurements

Angle resolved photoemission spectroscopy (ARPES) measurements were performed on 1uc-FeSe/STO samples using a He lamp (21.2 eV) and our 2D-HREELS analyzer along the $\Gamma\bar{M}$ direction, corresponding to the horizontal direction in the LEED pattern in Fig. 1(b). A parabolic electron band can be clearly observed in the spectrum [Fig. 1(c)]. Temperature-dependent EDCs symmetrized around k_F reveal the superconducting gap at 35 K is ~ 20 meV, which closes between 63 K and 73 K [Fig. 1(d)].

D. Surface Debye Temperature Measurements

LEED has been used routinely to determine the surface Debye temperature^{54–56}. According to the Debye-Waller theory^{57,58}, the coherent peak intensity will decay exponentially with increasing temperature due to the thermal vibrations. The time-averaged scattered intensity affected by thermal vibrations is given by⁵⁹

$$\begin{aligned} \langle I(S) \rangle &= \langle I_{\text{Bragg}} \rangle + \langle I_D \rangle \\ &= |f_0|^2 e^{-2M} \sum_i \sum_j e^{iS \cdot (r_i - r_j)} + \langle I_D \rangle, \end{aligned} \quad (1)$$

with

$$M = 8\pi^2 \langle u^2 \rangle \frac{\sin^2 \phi}{\lambda^2}, \quad (2)$$

TABLE I. Samples used in the HREELS study.

Labels	Substrate	Films	Substrate Preparation
treated STO	0.5% Nb-doped SrTiO ₃ (001)	-	950°C annealing and Se treatment
clean STO	0.5% Nb-doped SrTiO ₃ (001)	-	HF etching and 600°C annealing
clean STO (w/o Nb)	0.5% Nb-doped SrTiO ₃ (001)	40uc SrTiO ₃ (001) film (w/o Nb)	HF etching and 600°C annealing
1uc-FeSe/STO	0.5% Nb-doped SrTiO ₃ (001)	1uc FeSe films	950°C annealing and Se treatment
3uc-FeSe/STO	0.5% Nb-doped SrTiO ₃ (001)	3uc FeSe films	950°C annealing and Se treatment
10uc-FeSe/STO	0.5% Nb-doped SrTiO ₃ (001)	10uc FeSe films	950°C annealing and Se treatment
TiO ₂ (110)(w/o Nb)	rutile TiO ₂ (110)	-	900°C annealing
BaTiO ₃ (w/o Nb)	0.5% Nb-doped SrTiO ₃ (001)	40uc BaTiO ₃ (001) film (w/o Nb)	HF etching and 600°C annealing
STO(110) 2×8	0.5% Nb-doped SrTiO ₃ (110)	-	Ar ⁺ ion sputtering and 1470°C annealing
STO(110) 4×1	0.5% Nb-doped SrTiO ₃ (110)	-	Ar ⁺ ion sputtering and 1470°C annealing

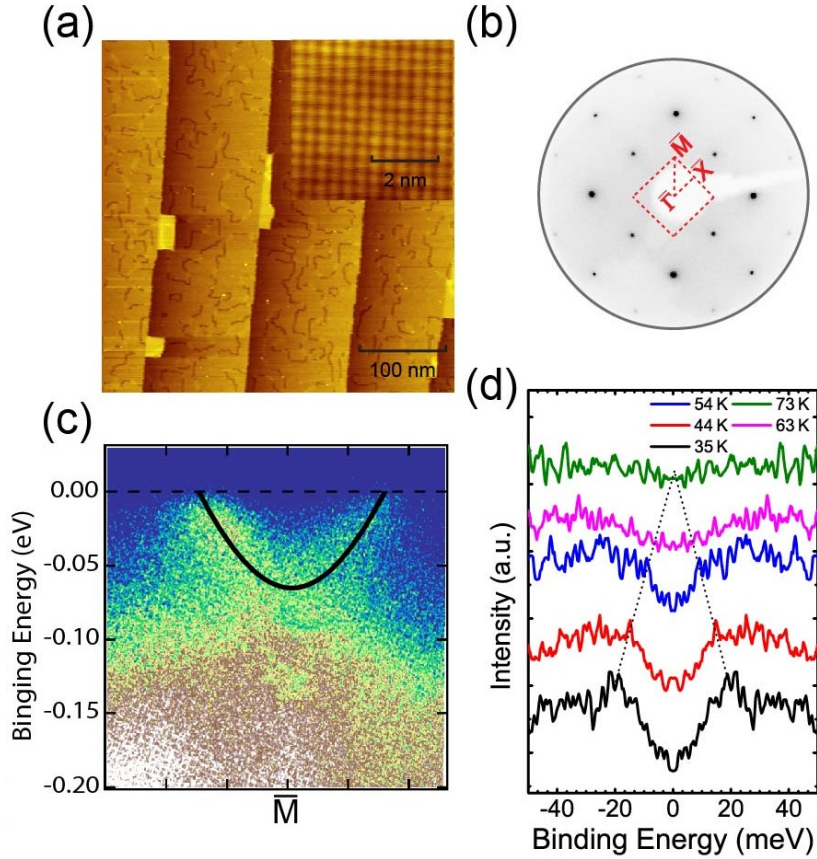


FIG. 1. (a) STM topography of 1uc-FeSe/STO sample (400×400 nm, 5.0 V/50 pA). inset: Atomically resolved STM topography of 1uc-FeSe/STO sample (5×5 nm, 0.4 V/100 pA). (b) LEED patterns of 1uc-FeSe/STO sample taken at 35 K with the primary energy of 80 eV. Red dashed lines represent the first surface Brillouin zone. (c) ARPES spectrum of 1uc-FeSe/STO, taken at 35 K along the $\Gamma\bar{M}$ direction and centered at \bar{M} . The photon energy is 21.2 eV. The black line represents the band fitting by a tight binding model⁵. (d) Plot of the evolution of the ARPES symmetrized energy distribution curves (EDCs) near k_F as a function of temperature, indicating the gap closes between 63 K and 73 K.

and

$$\langle u^2 \rangle = \frac{3\hbar^2 T}{mk_B \Theta^2}, \quad (3)$$

where f_0 is the structure factor, S is the diffraction vector ($k - k_0$), $\langle u^2 \rangle$ is the mean square displacement of the atoms' thermal vibrations from their equilibrium position parallel to S , λ is the wavelength of the scattered radiation, ϕ is the Bragg angle, k_B is the Boltzmann constant, m is the atomic mass, and Θ is the Debye temperature.

The first term $\langle I_{\text{Bragg}} \rangle$ in Eq. 1 shows that the Bragg intensity is reduced by a prefactor e^{-2M} . This prefactor is known as the Debye-Waller factor, containing the effect of the thermal vibrations of the atoms about their equilibrium position. Since the mean square of displacement from equilibrium will increase with increasing temperature [as shown in Eq. 2 and Eq. 3, M is proportional to T], the thermal vibrations reduces exponentially the intensity of the Bragg peaks⁶⁰. Accordingly, the temperature dependence of LEED spot intensity can be used to determine the Debye-Waller factor and calculate the surface Debye temperature. The second term $\langle I_D \rangle$ in Eq. 1 represents the first order temperature diffuse scattering, which induces a background in LEED pattern and should be subtracted before calculating the Debye temperature.

E. HREELS Measurements

As a surface-sensitive technique, HREELS is an ideal candidate to study the interfacial lattice dynamics of FeSe/STO systems. Compared with conventional HREELS, our recently developed 2D-HREELS system⁵³ can directly map a 2D energy-momentum dispersion over a very large momentum range without mechanically rotating sample, monochromator, or analyzer. Phonon spectra measurements were performed by the 2D-HREELS on 1uc, 3uc and 10uc-FeSe/STO samples.

In HREELS, a monochromatic electron beam with energy E_i incident on the sample surface may interact with surface elementary excitations such as phonons, and be scattered with the final energy E_f . The energy loss $E_{\text{loss}} = E_i - E_f$ represents the energy of surface excitations. In our HREELS measurements, the incident electron beam energies are $E_i = 50$ eV and 80 eV for the scattering direction along the $\Gamma\bar{X}$ and $\Gamma\bar{M}$ directions, respectively, and the incident angle (θ_i) is 60° with respect to the surface normal. The surface phonon momentum can be determined from the scattering angles by $q = \frac{\sqrt{2m_e E_i}}{\hbar} (\sin \theta_i - \sin \theta_f)$ when $E_{\text{loss}} \ll E_i$, where m_e is the electron mass, θ_i and θ_f are the angles of the incident and scattered electrons, respectively. The energy and momentum resolutions of HREELS in this study are $\Delta E \sim 3$ meV and $\Delta k \sim 0.01 \text{ \AA}^{-1}$, respectively.

For most samples, the HREELS measurements were carried out along both $\Gamma\bar{X}$ and $\Gamma\bar{M}$ directions with the sample temperature ranging from 35 K to 300 K.

F. First Principles Calculation Details

For the calculations of FeSe phonon dispersions, we use the frozen-phonon method as implemented in the phonopy code⁶¹ by performing density functional theory (DFT) calculations to extract the interatomic force constant matrix. The DFT calculations are performed using the plane wave projector augmented wave (PAW) method⁶² as implemented in the VASP code^{63,64}. The phonon dispersion calculated with the frozen-phonon method and VASP code (FP/VASP) is compared with the phonon dispersion calculated with the density functional perturbation theory (DFPT) method as implemented in the Quantum ESPRESSO package⁶⁵ (DFPT/QE), and they agree with each other well with a maximum difference less than 1 meV. In the DFPT/QE calculations, we use the plane wave ultrasoft pseudopotential method and the GBRV pseudopotential library⁶⁶. In both FP/VASP and DFPT/QE calculations, we take the exchange-correlation functional in the generalized gradient approximation (GGA) of Perdew-Burke-Ernzerhof (PBE) type⁶⁷.

In experiment the monolayer FeSe thin film is deposited on the SrTiO₃ substrate, which exerts strong tensile strain on the monolayer FeSe. To take into account this effect, in the calculations we set the in-plane lattice parameter $a = 3.905 \text{ \AA}$ for the monolayer FeSe thin film, the same as the lattice parameter for a bulk SrTiO₃ crystal. Lattice constants corresponding to the 3 and 10 unit cell FeSe films are extracted from Ref.26. We place a vacuum layer around 12 \AA in height above the monolayer FeSe before it is repeated in the c direction. Before phonon dispersion calculations, the internal atomic coordinates are relaxed until a force smaller than 1 meV/ \AA is found on each atom. We have performed phonon dispersion calculations for both nonmagnetic (NM) and checkerboard antiferromagnetic (cAFM) phases and find that the phonon dispersion of the cAFM phase quantitatively agrees with the EELS experiment much better than that of NM phase. For the VASP monolayer FeSe calculations $15 \times 15 \times 1$ k-point grids were used to relax the atoms in the unit cells and $3 \times 3 \times 1$ k-grids were used in $3 \times 3 \times 1$ supercells to compute the phonon dispersions. For the VASP bulk FeSe calculations $15 \times 15 \times 10$ k-point grids were used to relax the atoms in the unit cells and $3 \times 3 \times 3$ k-grids were used in $3 \times 3 \times 2$ supercells to compute the phonon dispersions. For all VASP calculations a 500 eV kinetic energy cutoff was employed.

III. RESULTS

A. Surface Phonon Spectra

The HREELS results are summarized in Fig. 2. Figure 2(a) is a schematic drawing of the FeSe layer on SrTiO₃. The FeSe lattice is consisted of Se-Fe-Se triple layers stacked by van der Waals forces, with the primitive unit cell containing two Fe atoms and two Se atoms. In each Se-Fe-Se triple layer, Fe atoms form a square lattice and Se atoms staggered above and below the Fe plane, as shown in Fig. 2(c). The film with 1uc thickness (5.5 \AA) corresponds to one Se-Fe-

Se triple layer. Figures 2(b) and 2(c) depict the vibrational modes of some relevant optical phonons at $q = 0$ of the STO and FeSe, respectively. To illustrate the phonon dispersions at 1uc-FeSe/STO surface, in Figs. 2(d) and 2(e), we show a typical 2D-HREELS energy-momentum mapping for the 1uc-FeSe/STO(001) sample along $\bar{\Gamma}\bar{X}$ direction at 36 K.

In a HREELS measurement, there are two scattering mechanisms⁶⁸. One is referred to as impact scattering, where the incident electrons are scattered by impacting with nuclei of the sample. In this mechanism, the penetration depth or free electron path of incident electrons (with the energy of 50 eV) is nearly three atomic layers, i.e., around one Se-Fe-Se triple layer (one unit cell thick in c direction of FeSe crystal). In this context, most the detected signals of FeSe phonons come from the topmost Se-Fe-Se layer of FeSe films. In the low energy range 0-40 meV (Fig. 3), five Fe- and Se-derived phonon branches are clearly observed: one acoustic branch with energy from 0 - 8 meV, and the other four optical branches with energies ranging from 18 - 40 meV. Another branch around 15 meV [$E_g(1)$ mode] has a very weak signal that is barely discernible in the second derivative image from the data at $T=35$ K. The energies of two bulk phonon modes determined from Raman scattering experiment⁴³ are also labeled at the $\bar{\Gamma}$ point in Figs. 2(d) and 2(e), indicating that the corresponding phonon energies of single layer FeSe films are similar to the bulk modes.

The other mechanism is called dipole scattering, where the incident electrons are scattered by dipole fields generated by ionic vibrations. The ultra-sensitivity to F-K phonons in HREELS measurements is due to this mechanism. In this case, the incident electrons may scatter outside the surface nuclei position, depending on the strength of the dipole field. The STO substrate has two obvious F-K surface phonons, labeled by α and β , which can generate strong electric fields and penetrate through FeSe films. The buried STO signal can be observed because the electrons in FeSe layers can not completely screen the electric field from the F-K phonons³⁹.

B. Thickness Independence of FeSe phonons

1. Surface Phonon Dispersions

To check the substrate effect on the FeSe phonons as a function of film thickness, phonon spectra of 3uc and 10uc-FeSe/STO are also measured, and compared with 1uc-FeSe/STO in Fig. 4. Phonon energies and dispersions of thick FeSe films show no obvious difference (within the energy resolution) compared to the phonons of 1uc-FeSe films at 35 K. This indicates that charge transfer or other interfacial coupling such as tensile strain does not renormalize the phonon dispersions. As shown by the energy distribution curves (EDCs) at different momentum points in Figs. 4(d) - 4(f), the linewidths of FeSe phonons in different thickness samples are also similar and all close to the instrument resolution. Since the linewidths and dispersion profiles of phonons can reflect the strength of mode-specific EPC⁶⁹, the similar linewidth and dispersion for different thickness films provide

evidence that the EPC from FeSe phonons is not altered by the existence of substrate or the thickness of the film. Thus, FeSe phonons are not directly related to the interfacial T_C enhancement.

2. Surface Debye Temperature

The thickness independence of FeSe phonons is further confirmed by the measurements of the surface Debye temperature. To check the lattice contribution in electron pairing, Debye temperature (Θ) is a vital factor in the McMillan equation⁷⁰ and sets the energy scale for T_C in the standard BCS approach in bulk iron pnictides^{46,71}. We use the surface sensitive probe LEED to determine the surface Debye temperature (see Section II D for details of this technique).

We performed LEED I/V measurements to determine the positions of the Bragg peaks (Bragg positions) for three different samples: STO, 1uc-FeSe/STO and 10uc-FeSe/STO as shown in Fig. 5(a). To acquire the Debye-Waller factor, LEED I/V spectra measurements were performed at different temperatures from 35 - 300 K. Figures 5(b) and 5(c) show the LEED patterns of 1uc-FeSe/STO at 35 K and 300 K respectively. Clearly, the spot intensity at 35 K [Fig. 5(b)] is much stronger than that at 300 K [Fig. 5(c)] because of the reduced thermal vibrations. The spot intensities as a function of temperature at a given voltage (Bragg positions) are plotted and fitted exponentially with $I(T) \propto e^{-2M}$ to determine the Debye temperature. As an example of the analysis, the LEED (00) spot intensity for 1uc-FeSe/STO at 220 eV is shown in Fig. 5(d), giving $\Theta(220\text{eV}) = 253$ K. In the fitting, we approximate the Bragg angle ϕ as 90° , and m the average atomic mass of FeSe. The average surface Debye temperature measured from different Bragg positions is $\Theta_{1\text{uc}} \sim 249 \pm 33$ K for 1uc-FeSe/STO and $\Theta_{10\text{uc}} \sim 230 \pm 33$ K for 10uc-FeSe/STO, showing no obvious difference within the statistical error. The surface Debye temperatures for the two different film thicknesses are both located in the range of reported values for bulk FeSe, from 210 K (measured by specific heat⁴⁷) to 285 K (measured by ⁵⁷Fe nuclear inelastic scattering⁴⁵).

C. Changes of Substrate Phonons

In stark contrast to the unflappable FeSe phonons, the F-K phonons of STO substrate respond to every change in the system. As shown in Fig. 6 and Fig. 7, the phonon spectra of the F-K modes for various samples are plotted for comparison. The F-K phonons from the 1uc-FeSe/STO surface show several important features: (1) appearance of new energy loss modes; (2) dramatic temperature dependence; and (3) linewidth broadening compared to the F-K modes of clean STO.

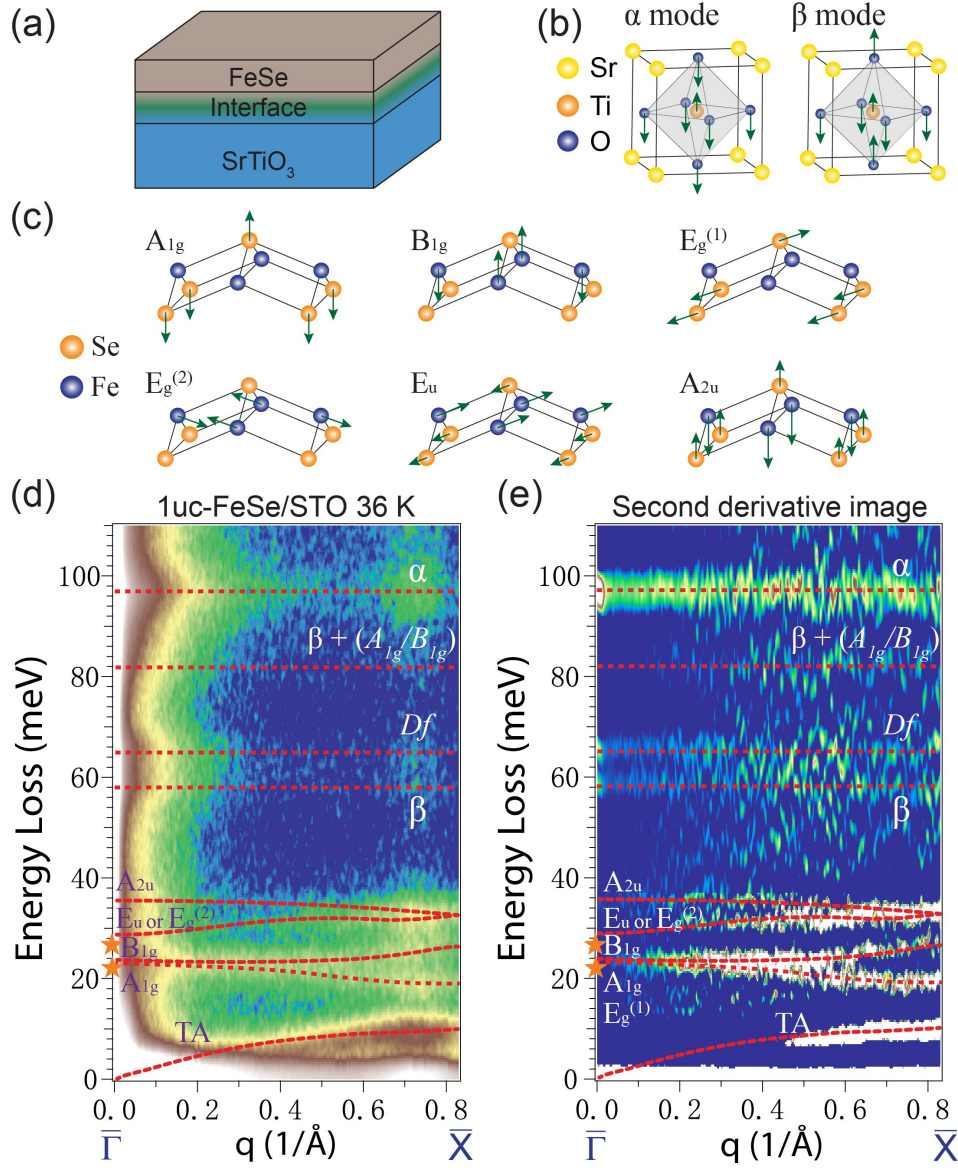


FIG. 2. (a) Schematic structure of the FeSe film on STO substrate. (b) Illustration of ionic vibrations of F-K phonons in STO. (c) Illustration of ionic vibrations of phonons in FeSe at $\bar{\Gamma}$ point. (d) Energy-momentum mapping of 2D HREELS measurements of 1uc-FeSe/STO samples along $\bar{\Gamma}\bar{X}$ direction at 35 K, where red solid lines are guides to the eye. Orange stars label the A_{1g} mode (22.6 meV) and B_{1g} mode (25.6 meV) measured by Raman scattering at 7 K⁴³. (e) Second derivative image of (d).

1. Appearance of new energy loss modes

The first feature is the appearance of new energy loss modes, *Df* and $\beta + A_{1g}/B_{1g}$, as shown in Figs. 6(b), 6(c) and Figs. 7(a), 7(b). It turns out that the *Df* originates from Nb-induced defects in STO substrate and the $\beta + A_{1g}/B_{1g}$ mode is an overtone of β mode in STO and A_{1g} or B_{1g} mode in FeSe films.

To illuminate the origin of the new energy loss modes, all energy loss modes observed on clean STO (w/o Nb) surface are labeled in Fig. 6(a) and summarized in Table II. There are 4 optical phonon modes and 4 overtones. The overtone

of $\chi + \beta$ modes can also be observed on treated STO surface as shown in Fig. 6(b). After the growth of FeSe films, A_{1g} and B_{1g} modes from Fe- and Se-derived phonons are also involved into the overtone [labeled as $\beta + A_{1g}/B_{1g}$ in Fig. 6(c)] with the energy similar to $\chi + \beta$ mode. Thus, thicker FeSe films have larger intensity ratio $I(\beta + A_{1g}/B_{1g})/I(\alpha)$, as shown in Fig. 7(b).

For STO with Nb doping, a new energy loss mode with 65.3 meV labeled by *Df* emerges as shown Fig. 6(b), while this *Df* mode does not exist in samples without Nb-doping. Thus the *Df* mode should originate from Nb-induced defects in STO substrate. It is well-known that the superconducting

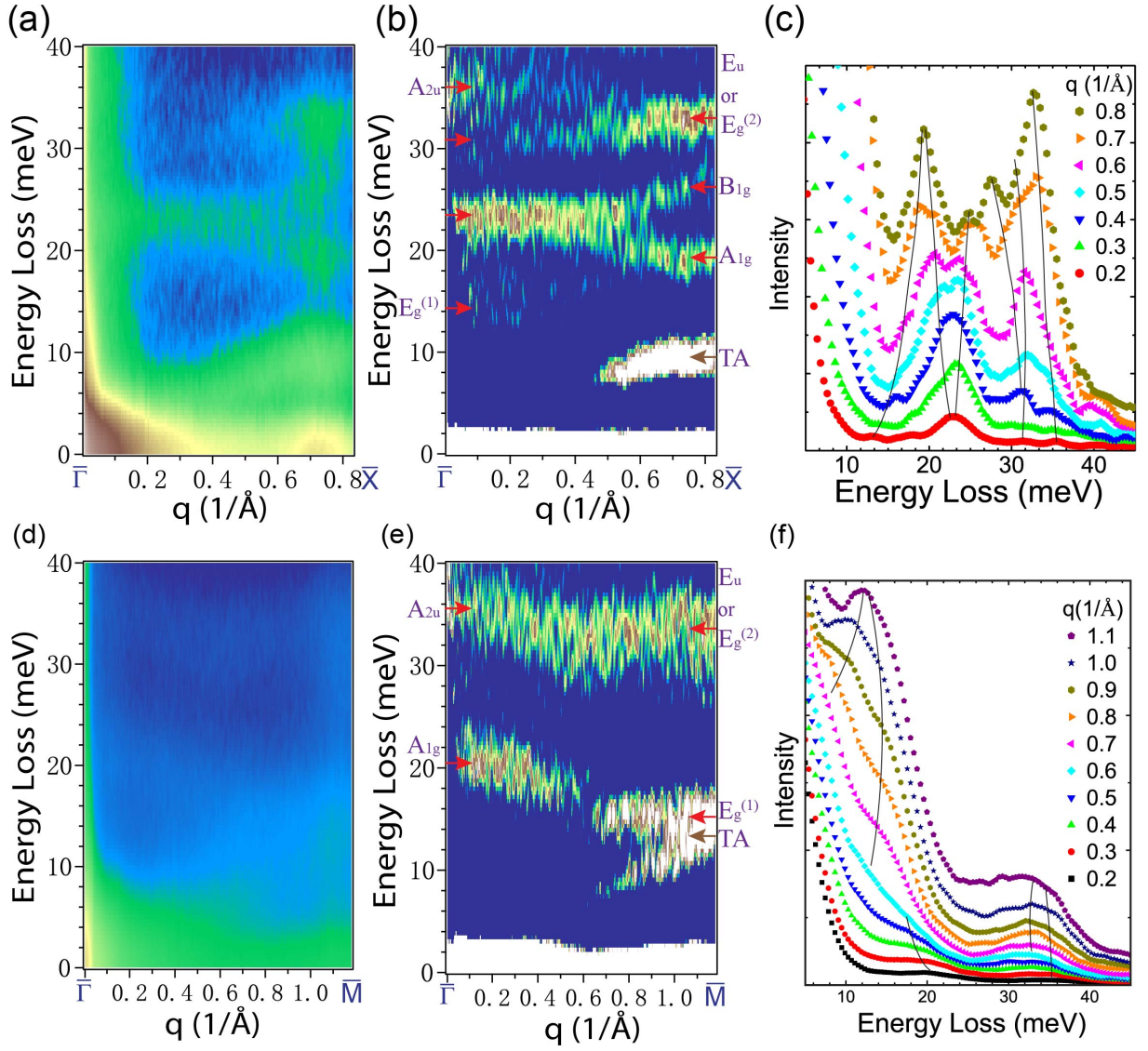


FIG. 3. (a) Energy-momentum mapping (0 - 40 meV) of 2D HREELS measurements of 1uc-FeSe/STO samples along $\overline{\Gamma X}$ direction at 35 K. (b) Second derivative image of (a). (c) Momentum dependent EDCs of (a), where black lines are only guides. (d) - (f) Corresponding results along $\overline{\Gamma M}$ direction.

behavior of FeSe films does not depend on Nb-doping of the STO substrate, thus the Df mode is not related to the T_C in 1uc-FeSe/STO samples.

2. Dramatic temperature dependence

The second feature is the dramatic temperature dependence in phonon energy of F-K phonons as shown in Fig. 6(c). From the comparison between Figs. 6(b) and 6(c), the line profile of the energy loss spectra is different with or without the growth of FeSe films. The difference of temperature-dependent line profile contains two part of contributions: (1) overtone of β and A_{1g}/B_{1g} ; (2) energy softening caused by anharmonic phonon-phonon interaction.

First, as observed from Figs. 6(b) and 6(c), the intensity of A_{1g} and B_{1g} modes in FeSe films increase with increasing temperature, thus the intensity of the overtone $\beta + A_{1g}/B_{1g}$ becomes stronger at high temperature than that of $\chi + \beta$ on treated STO surface.

Second, on 1uc-FeSe/STO surface [Fig. 6(d)], the energy of α mode is strongly temperature-dependent, softening from ~ 97 meV at 35 K to ~ 92 meV at 254 K. In contrast, it is almost temperature-independent on all STO substrates without FeSe. This energy shift accompanied with linewidth broadening is due to the anharmonic phonon-phonon interaction, which will lead to the decay of F-K modes into other low energy FeSe phonons. The low energy FeSe phonons provide more possible decay channels for the F-K phonons³⁹. As an example in MgB_2 ⁷², the anharmonic phonon-phonon interac-

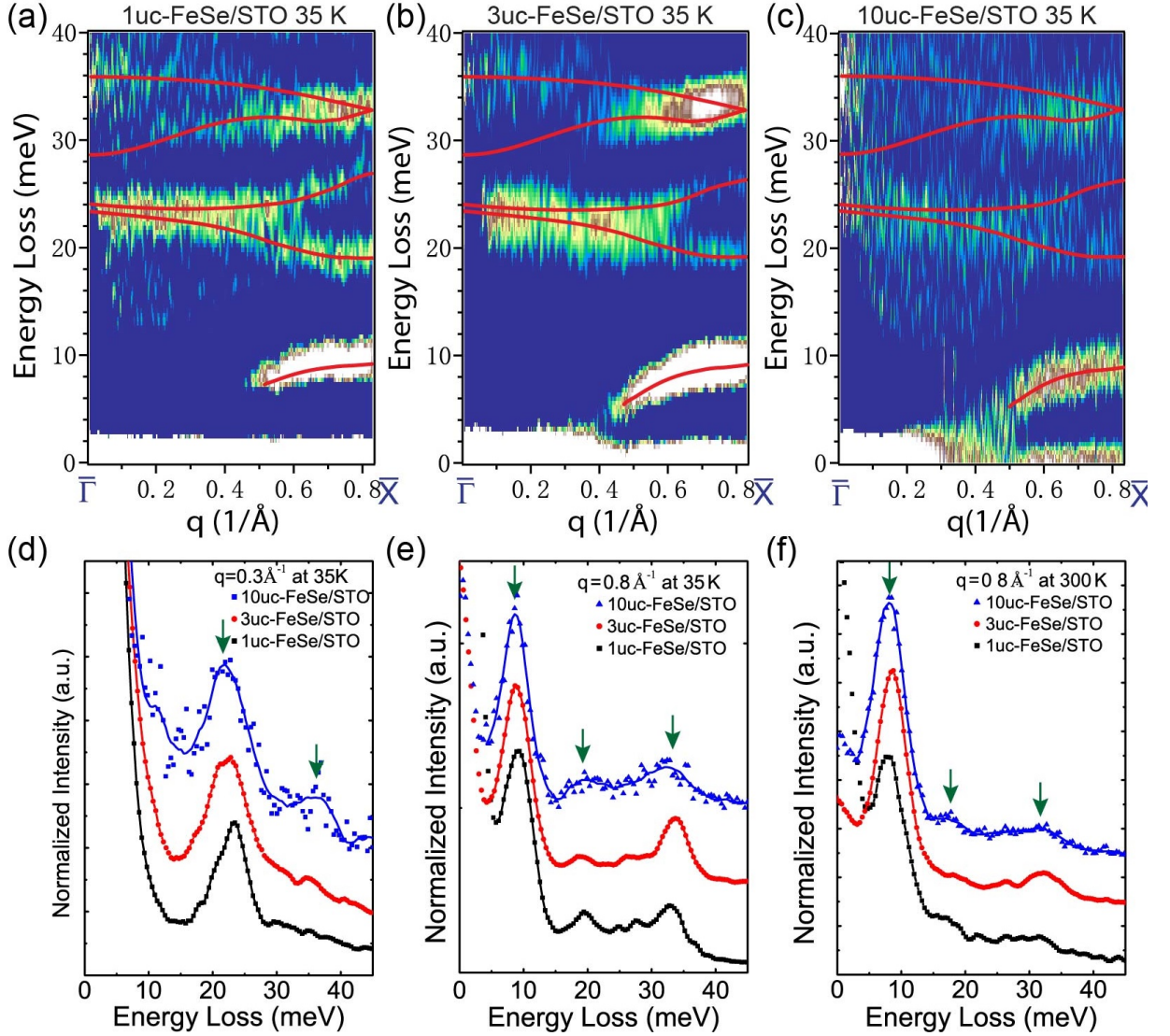


FIG. 4. Phonon dispersions of low energy FeSe phonons of (a) 1uc-FeSe/STO, (b) 3uc-FeSe/STO and (c) 10uc-FeSe/STO samples at 35 K, where the colored images are the second derivative energy-momentum mappings of 2D HREELS measurements, and red solid lines are guides to eyes. EDCs from different samples are compared at different momentum points: (d) $q = 0.3 \text{ Å}^{-1}$ at 35 K, (e) $q = 0.8 \text{ Å}^{-1}$ at 35 K and (f) $q = 0.8 \text{ Å}^{-1}$ at 300 K.

TABLE II. The assignments of energy loss modes at $\bar{\Gamma}$ point of clean STO (w/o Nb) surface at 35K.

Phonon Mode	Phonon Energy (meV)	Overtone	Overtone Energy (meV)
χ	22.8	$\chi + \beta$	84.2
ϕ	32.9	$\chi + \alpha$	115.9
β	58.9	$\beta + \alpha$	152.2
α	94.6	2α	188.1

tion can adjust the band structure and then generate strong EPC. Thus, F-K phonons from the STO substrate and interfacial electronic structure might be critical to reveal the interfacial EPC.

3. Linewidth broadening compared to the F-K modes of clean STO

The third feature is that the linewidths (Γ_{ep}) of F-K phonon modes associated with 1uc-FeSe/STO are larger than those

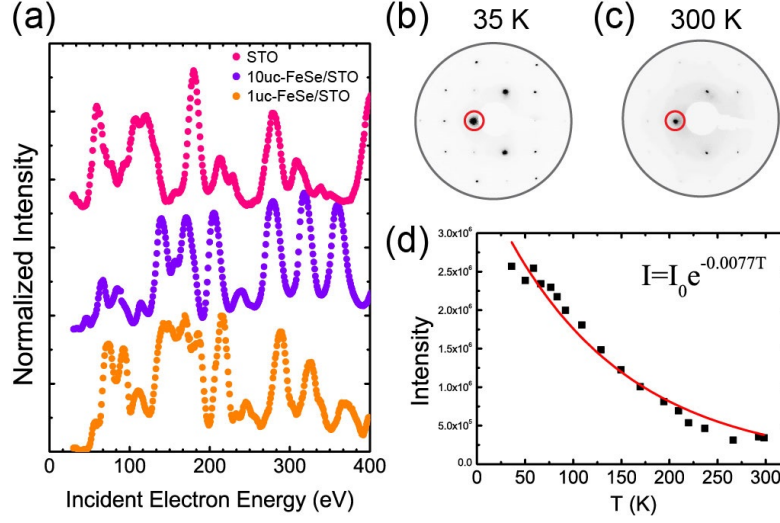


FIG. 5. (a) LEED I/V spectra at 35 K of the (00) spot for STO (pink), 1uc-FeSe/STO (purple) and 10uc-FeSe/STO (orange). (b) LEED patterns for 1uc-FeSe/STO at 35 K and (c) 300 K, for a primary energy of 140 eV. The red circles indicate the (00) spot. (d) The intensity of the (00) spot of 1uc-FeSe/STO as a function of temperature with the primary energy of 220 eV.

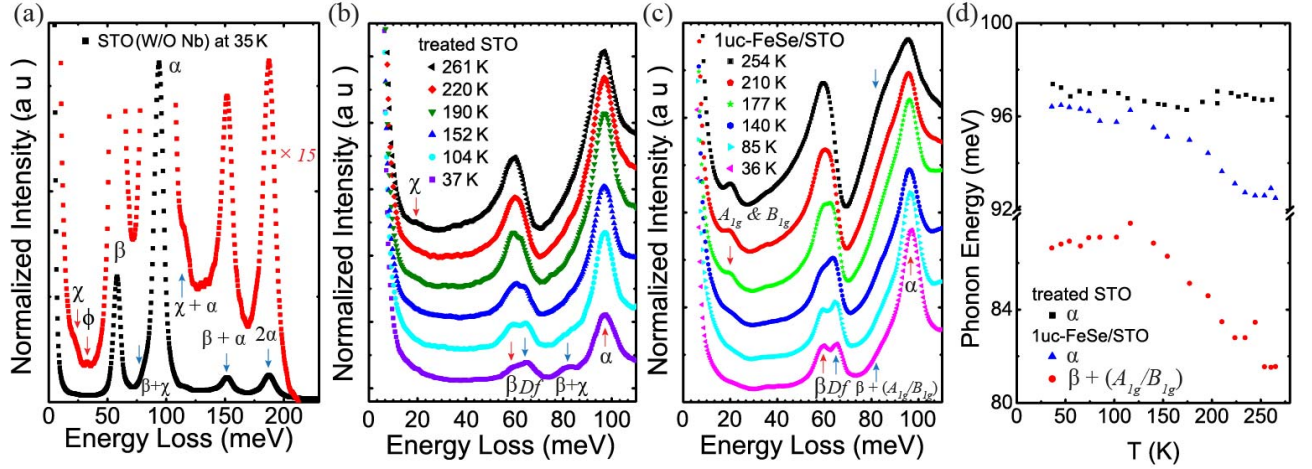


FIG. 6. (a) EDCs of phonon spectra at $\bar{\Gamma}$ point of clean STO(001) (w/o Nb) at 35K. Red data are expanded by 15 times from the raw data in black. (b) Temperature-dependent EDCs of treated STO at $\bar{\Gamma}$ point. (c) Temperature-dependent EDCs of 1uc-FeSe/STO at $\bar{\Gamma}$ point. (d) Plot of the energies of several modes as a function of temperature for treated STO and 1uc-FeSe/STO at $\bar{\Gamma}$ point.

TABLE III. Energies and line-width of F-K modes at 35K. Γ_{ep} is the linewidth [full width at half maximum (FWHM)] in meV, after deconvoluting the elastic peak width $\Gamma = 5.6$ meV. All the substrates in this table are Nb-doped STO unless stated otherwise.

	mode	clean STO (w/o Nb)	clean STO	1uc-FeSe/STO	3uc-FeSe/STO	10uc-FeSe/STO
Energy (meV)	α	94.1	96.5	96.9	96.4	93.4
	β	59.0	58.8	59.3	58.3	58.6
Linewidth Γ_{ep} (meV)	α	6.0	7.0	7.4-10.2 ¹	9.7	13.7
	β	1.6	2.9	1.8-3.4 ¹	5.6	8.3

¹ The linewidth of 1uc-FeSe/STO varies with the substrate batches and film growth conditions. The average value is 9.1 ± 1.5 meV for α mode, and 2.4 ± 0.9 meV for β mode.

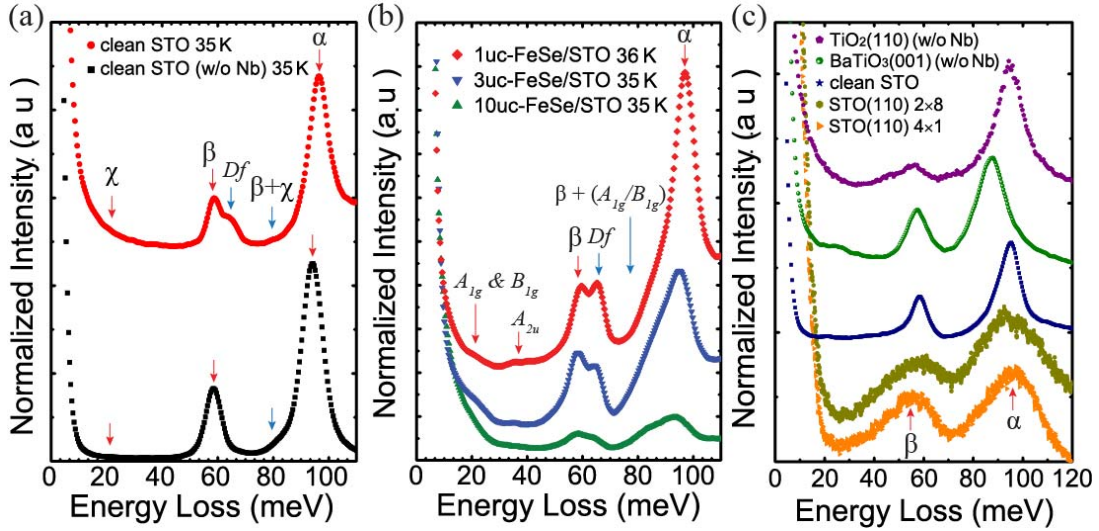


FIG. 7. (a) Comparison of EDCs of phonon spectra at $\bar{\Gamma}$ point of clean STO(001) (w/o Nb) and clean STO(001). (b) Comparison of EDCs of phonon spectra at $\bar{\Gamma}$ point of 1uc, 3uc and 10uc-FeSe/STO. (c) Energy loss spectra at $\bar{\Gamma}$ point of several typical oxide surfaces: rutile $\text{TiO}_2(110)$ (w/o Nb), BaTiO_3 (w/o Nb), $\text{STO}(110) 2 \times 8$, $\text{STO}(110) 4 \times 1$, and clean STO, all at room temperature.

of clean STO(001) as illustrated in Table.III. The phonon linewidth broadening can be either from EPC or anharmonic phonon-phonon interaction. The phonon-phonon interactions are strongly temperature dependent and can be neglected at low temperature. So the strength of the mode-specific EPC is approximately proportional to the phonon linewidth at 35 K. After the growth of FeSe film, the linewidth of α mode (9.1 ± 1.5 meV) is broadened comparing to that of clean STO (6.5 ± 0.7 meV). This linewidth broadening is a signature of EPC enhancement, implying the penetrated F-K phonons do interact with electrons in FeSe films. While the broadening of the β mode is less obvious than the α mode, indicating a relatively weaker coupling between electrons and the β mode. However, this broadening at $q = 0$ is currently a challenge for theory^{73,74} of interfacial e-ph coupling, rooted in Migdal-Eliashberg-based approaches with dynamics screening.

Additionally thicker FeSe films accompany with larger linewidth, also shown in Table.III. Since the electric field generated by STO F-K phonons can penetrate into FeSe films, F-K phonons from substrate STO interact with all the electrons in FeSe films. The total amount of electrons in FeSe films increase with increasing thickness, thus the linewidth broadening of the F-K phonon is an additive effect layer by layer with the growth of FeSe films. As a result, thicker FeSe films will always show a larger phonon linewidth than that of thinner films. Electrons in the FeSe layer closest to FeSe/STO interface contribute the largest electron-phonon coupling. This contribution becomes smaller in the layers further from the interface, because the electric field decays exponentially inside the FeSe films³⁹.

If EPC of F-K phonons play a vital role on the superconductivity of FeSe films, these high energy F-K phonons should also be present in a variety of oxide substrates. Surface phonons on other oxides, such as rutile $\text{TiO}_2(110)$,

$\text{BaTiO}_3(001)$ and $\text{SrTiO}_3(110)$ ⁵², are measured and shown in Fig. 7(c). As a ubiquitous characteristic of oxides⁷⁵, all those sample surfaces have F-K phonons with similar energies that are accompanied with strong electric field, independent of the crystal orientation, surface reconstruction, crystal symmetry, or lattice constant. These facts establish the critical role played by oxide F-K phonons on the T_C enhancement at FeSe/oxides interface. Thus the specific F-K phonon energy scale ~ 100 meV and the metal-oxygen chemical bond strength should be vital for the interfacial T_C enhancement.

D. First-principles Calculations and the Magnetic Structure in FeSe films

Although the F-K phonons from STO substrate play an essential role, the T_C enhancement in FeSe-derived systems without the substrate indicate that these modes do not act alone. Magnetic interactions have been always speculated as one of the most possible candidate origins of the pairing in FeSe bulk. However, the existence of magnetic interaction in FeSe/STO is still elusive, due to the limitation of the experimental techniques to measure the magnetic ordering of ultrathin films. In this study our first-principles calculation results show that the AFM correlation in FeSe is indispensable to quantitatively reproduce the experimental phonon dispersions in the ultrathin FeSe films.

First-principles calculations are performed to calculate the dispersions of the Fe- and Se-derived phonons in the single layer FeSe film. The technical details of computation have been given in Section II F. In the calculations, when the AFM spin configuration on Fe lattice is taken into account, the total energy per Fe is 103 meV lower compared to the non-magnetic configuration. Moreover, the AFM results exhibit

significant phonon energy renormalization and provide much better consistency with our experimental results than these from nonmagnetic structure, as shown in Figs. 8(a) and 8(b). In addition, these figures show that the AFM calculations agree better with Raman scattering at 7 K⁴³ compared to the NM calculations. We note that phonon bands 6 and 7 (counting from the low energy bands) at $\bar{\Gamma}$ in the AFM and NM calculations correspond to the $A_{1g}(\text{Se})$ and $B_{1g}(\text{Fe})$ modes respectively. These results verify the existence of AFM correlations in single layer FeSe films, which implies spin fluctuation is still important to the superconductivity of single layer FeSe films, similar to the case in FeSe bulk^{40,41}. As seen from the comparisons in Figs. 8(c) and 8(d), film thicknesses and lattice constant cannot significantly modify the energies of FeSe phonons, which is also consistent with the HREELS experimental results. The unflappable FeSe phonons for different film thickness suggest that similar magnetic moments or AFM correlations are possessed by Fe atoms for various thickness FeSe films, since the phonon energy directly reflects the AFM ground state of FeSe as discussed above. As a result, from a similar strength of AFM correlations, the spin fluctuations are not expected to be enhanced from the FeSe bulk to thin films. Rather than directly increasing the AFM correlation in the films to enhance the superconductivity mediated by the spin fluctuations, the F-K phonons of STO must take effect by itself or in an indirect way to give a significantly higher T_c , which requires further theoretical and experimental investigations.

IV. CONCLUSION

In summary, although the electronic structure is tuned by STO substrates, lattice dynamics of FeSe films are unaffected. The phonon energy dispersions associated with the Fe and Se atoms are not only temperature-independent but also thickness-independent. In contrast, the F-K phonons of STO substrate are strongly temperature-dependent in line profile, and change drastically with or without FeSe films. Therefore,

if there is EPC which could enhance the interfacial superconductivity, it must be the interaction between the F-K modes of the substrate (with electric field penetrating into the film) and electrons in the FeSe film. Coupling to the FeSe derived phonon modes does not increase the superconducting T_c . Moreover, combination of the calculations and experimental phonon dispersions strongly suggest the existence of AFM correlations in 1uc-FeSe/STO, which is also verified to be thickness-independent. Since the superconductivity pairing mechanism of bulk FeSe is still elusive, how the F-K phonon modes in the substrates enhance the existing pairing still needs to be elucidated in future studies.

ACKNOWLEDGEMENTS

The work was supported by the National Natural Science Foundation of China (No. 11634016), the National Key R&D Program of China (No. 2017YFA0303600). X. Z. was partially supported by the Youth Innovation Promotion Association of Chinese Academy of Sciences (CAS), and the Open Research Fund Program of the State Key Laboratory of Low-Dimensional Quantum Physics. Y. W. was supported by the U.S. Department of Energy, Office of Basic Energy Sciences, Materials Sciences and Engineering Division. Part of this work (T. B.) was conducted at the Center for Nanophase Materials Sciences, sponsored by the Scientific User Facilities Division (SUFD), Basic Energy Sciences (BES), DOE, under contract with UT-Battelle. CPU time was provided in part by resources supported by the University of Tennessee and Oak Ridge National Laboratory Joint Institute for Computational Sciences (<http://www.jics.utk.edu>). This research used resources of the National Energy Research Scientific Computing Center, a DOE Office of Science User Facility supported by the Office of Science of the U.S. DOE under Contract No. DE-AC02-05CH11231. J. Z. was partially supported by U.S. NSF through Grant No. DMR 1608865, and the sabbatical program of the Institute of Physics CAS.

* xtzhz@iphy.ac.cn

† jdguo@iphy.ac.cn

¹ Q.-Y. Wang, Z. Li, W.-H. Zhang, Z.-C. Zhang, J.-S. Zhang, W. Li, H. Ding, Y.-B. Ou, P. Deng, K. Chang, J. Wen, C.-L. Song, K. He, J.-F. Jia, S.-H. Ji, Y.-Y. Wang, L.-L. Wang, X. Chen, X.-C. Ma, and Q.-K. Xue, Chinese Physics Letters **29**, 037402 (2012).

² W.-H. Zhang, Y. Sun, J.-S. Zhang, F.-S. Li, M.-H. Guo, Y.-F. Zhao, H.-M. Zhang, J.-P. Peng, Y. Xing, H.-C. Wang, T. Fujita, A. Hirata, Z. Li, H. Ding, C.-J. Tang, M. Wang, Q.-Y. Wang, K. He, S.-H. Ji, X. Chen, J.-F. Wang, Z.-C. Xia, L. Li, Y.-Y. Wang, J. Wang, L.-L. Wang, M.-W. Chen, Q.-K. Xue, and X.-C. Ma, Chinese Physics Letters **31**, 017401 (2014).

³ W. Zhang, Z. Li, F. Li, H. Zhang, J. Peng, C. Tang, Q. Wang, K. He, X. Chen, L. Wang, X. Ma, and Q.-K. Xue, Phys. Rev. B **89**, 060506 (2014).

⁴ D. Liu, W. Zhang, D. Mou, J. He, Y.-B. Ou, Q.-Y. Wang, Z. Li, L. Wang, L. Zhao, S. He, *et al.*, Nature communications **3**, 931

(2012).

⁵ J. Lee, F. Schmitt, R. Moore, S. Johnston, Y.-T. Cui, W. Li, M. Yi, Z. Liu, M. Hashimoto, Y. Zhang, *et al.*, Nature **515**, 245 (2014).

⁶ S. Tan, Y. Zhang, M. Xia, Z. Ye, F. Chen, X. Xie, R. Peng, D. Xu, Q. Fan, H. Xu, *et al.*, Nature materials **12**, 634 (2013).

⁷ J.-F. Ge, Z.-L. Liu, C. Liu, C.-L. Gao, D. Qian, Q.-K. Xue, Y. Liu, and J.-F. Jia, Nature materials **14**, 285 (2015).

⁸ F.-C. Hsu, J.-Y. Luo, K.-W. Yeh, T.-K. Chen, T.-W. Huang, P. M. Wu, Y.-C. Lee, Y.-L. Huang, Y.-Y. Chu, D.-C. Yan, *et al.*, Proceedings of the National Academy of Sciences **105**, 14262 (2008).

⁹ D.-H. Lee, Chinese Physics B **24**, 117405 (2015).

¹⁰ I. Bozovic and C. Ahn, Nature Physics **10**, 892 (2014).

¹¹ D. Huang and J. E. Hoffman, Annual Review of Condensed Matter Physics **8**, 311 (2017).

¹² Z. Wang, C. Liu, Y. Liu, and J. Wang, Journal of Physics: Condensed Matter **29**, 153001 (2017).

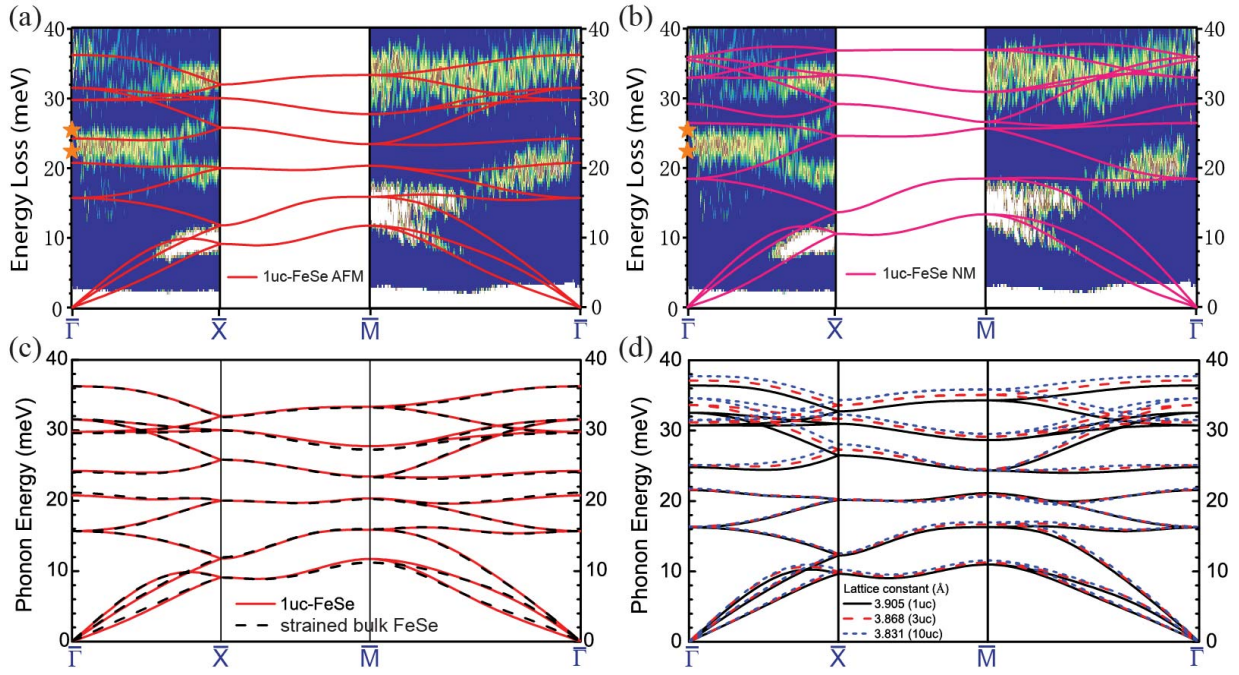


FIG. 8. Comparison between experimental data and theoretical calculations for single layer FeSe films, (a) with checkerboard AFM spin configuration on Fe lattice, and (b) without magnetic structure on Fe lattice. Orange stars label the A_{1g} mode (22.6 meV) and B_{1g} mode (25.6 meV) measured by Raman scattering at 7 K⁴³. (c) Comparison between theoretical results for single layer and strained bulk FeSe, both with AFM spin configuration on Fe lattice with lattice constant $a=3.905$ Å (d) Comparison between theoretical results for bulk FeSe with the lattice constants of 1uc, 3uc and 10uc-FeSe films respectively, both with AFM spin configuration on Fe lattice. Lattice constants used in theoretical calculations are extracted from Ref.26.

- ¹³ L. Wang, X. Ma, and Q.-K. Xue, *Superconductor Science and Technology* **29**, 123001 (2016).
- ¹⁴ W. Zhao, M. Li, C.-Z. Chang, J. Jiang, L. Wu, C. Liu, Y. Zhu, J. S. Moodera, and M. H. Chan, *arXiv preprint arXiv:1701.03678* (2017).
- ¹⁵ S. He, J. He, W. Zhang, L. Zhao, D. Liu, X. Liu, D. Mou, Y.-B. Ou, Q.-Y. Wang, Z. Li, *et al.*, *Nature materials* **12**, 605 (2013).
- ¹⁶ J. He, X. Liu, W. Zhang, L. Zhao, D. Liu, S. He, D. Mou, F. Li, C. Tang, Z. Li, *et al.*, *Proceedings of the National Academy of Sciences* **111**, 18501 (2014).
- ¹⁷ X. Lu, N. Wang, H. Wu, Y. Wu, D. Zhao, X. Zeng, X. Luo, T. Wu, W. Bao, G. Zhang, F. Huang, Q. Huang, and X. Chen, *Nature Materials* **14**, 325 (2015).
- ¹⁸ L. Zhao, A. Liang, D. Yuan, Y. Hu, D. Liu, J. Huang, S. He, B. Shen, Y. Xu, X. Liu, L. Yu, G. Liu, H. Zhou, Y. Huang, X. Dong, F. Zhou, K. Liu, Z. Lu, Z. Zhao, C. Chen, Z. Xu, and X. J. Zhou, *Nature Communications* **7**, 10608 (2016).
- ¹⁹ J. Seo, B. Kim, B. Kim, J. Jeong, J. Ok, J. S. Kim, J. Denlinger, S.-K. Mo, C. Kim, and Y. Kim, *Nature Communications* **7**, 11116 (2016).
- ²⁰ C. Wen, H. Xu, C. Chen, Z. Huang, X. Lou, Y. Pu, Q. Song, B. Xie, M. Abdel-Hafiez, D. Chareev, *et al.*, *Nature communications* **7**, 10840 (2016).
- ²¹ Y. Miyata, K. Nakayama, K. Sugawara, T. Sato, and T. Takahashi, *Nature materials* **14**, 775 (2015).
- ²² C.-L. Song, H.-M. Zhang, Y. Zhong, X.-P. Hu, S.-H. Ji, L. Wang, K. He, X.-C. Ma, and Q.-K. Xue, *Phys. Rev. Lett.* **116**, 157001 (2016).
- ²³ J. Shiogai, Y. Ito, T. Mitsuhashi, T. Nojima, and A. Tsukazaki, *Nature Physics* **12**, 42 (2015).
- ²⁴ B. Lei, J. H. Cui, Z. J. Xiang, C. Shang, N. Z. Wang, G. J. Ye, X. G. Luo, T. Wu, Z. Sun, and X. H. Chen, *Phys. Rev. Lett.* **116**, 077002 (2016).
- ²⁵ K. Hanzawa, H. Sato, H. Hiramatsu, T. Kamiya, and H. Hosono, *Proceedings of the National Academy of Sciences* **113**, 3986 (2016).
- ²⁶ R. Peng, X. P. Shen, X. Xie, H. C. Xu, S. Y. Tan, M. Xia, T. Zhang, H. Y. Cao, X. G. Gong, J. P. Hu, B. P. Xie, and D. L. Feng, *Phys. Rev. Lett.* **112**, 107001 (2014).
- ²⁷ F. Li, Q. Zhang, C. Tang, C. Liu, J. Shi, C. Nie, G. Zhou, Z. Li, W. Zhang, C.-L. Song, K. He, S. Ji, S. Zhang, L. Gu, L. Wang, X.-C. Ma, and Q.-K. Xue, *2D Materials* **3**, 024002 (2016).
- ²⁸ K. Zou, S. Mandal, S. D. Albright, R. Peng, Y. Pu, D. Kumah, C. Lau, G. H. Simon, O. E. Dagdeviren, X. He, I. Božović, U. D. Schwarz, E. I. Altman, D. Feng, F. J. Walker, S. Ismail-Beigi, and C. H. Ahn, *Phys. Rev. B* **93**, 180506 (2016).
- ²⁹ R. Peng, H. Xu, S. Tan, H. Cao, M. Xia, X. Shen, Z. Huang, C. Wen, Q. Song, T. Zhang, *et al.*, *Nature communications* **5**, 5044 (2014).
- ³⁰ P. Zhang, X.-L. Peng, T. Qian, P. Richard, X. Shi, J.-Z. Ma, B. B. Fu, Y.-L. Guo, Z. Q. Han, S. C. Wang, L. L. Wang, Q.-K. Xue, J. P. Hu, Y.-J. Sun, and H. Ding, *Phys. Rev. B* **94**, 104510 (2016).
- ³¹ G. Zhou, D. Zhang, C. Liu, C. Tang, X. Wang, Z. Li, C. Song, S. Ji, K. He, L. Wang, X. Ma, and Q.-K. Xue, *Applied Physics Letters* **108**, 202603 (2016).
- ³² H. Ding, Y.-F. Lv, K. Zhao, W.-L. Wang, L. Wang, C.-L. Song, X. Chen, X.-C. Ma, and Q.-K. Xue, *Phys. Rev. Lett.* **117**, 067001 (2016).
- ³³ S. N. Rebec, T. Jia, C. Zhang, M. Hashimoto, D.-H. Lu, R. G. Moore, and Z.-X. Shen, *Phys. Rev. Lett.* **118**, 067002 (2017).

- ³⁴ C. Tang, C. Liu, G. Zhou, F. Li, H. Ding, Z. Li, D. Zhang, Z. Li, C. Song, S. Ji, K. He, L. Wang, X. Ma, and Q.-K. Xue, *Phys. Rev. B* **93**, 020507 (2016).
- ³⁵ S. Coh, M. L. Cohen, and S. G. Louie, *New Journal of Physics* **17**, 073027 (2015).
- ³⁶ Y. Wang, A. Linscheid, T. Berlijn, and S. Johnston, *Phys. Rev. B* **93**, 134513 (2016).
- ³⁷ B. Li, Z. W. Xing, G. Q. Huang, and D. Y. Xing, *Journal of Applied Physics* **115**, 193907 (2014), <http://dx.doi.org/10.1063/1.4876750>.
- ³⁸ L. Rademaker, Y. Wang, T. Berlijn, and S. Johnston, *New Journal of Physics* **18**, 022001 (2016).
- ³⁹ S. Zhang, J. Guan, X. Jia, B. Liu, W. Wang, F. Li, L. Wang, X. Ma, Q. Xue, J. Zhang, E. W. Plummer, X. Zhu, and J. Guo, *Phys. Rev. B* **94**, 081116 (2016).
- ⁴⁰ Q. Wang, Y. Shen, B. Pan, Y. Hao, M. Ma, F. Zhou, P. Steffens, K. Schmalzl, T. Forrest, M. Abdel-Hafiez, *et al.*, *Nature materials* **15**, 159 (2016).
- ⁴¹ Q. Wang, Y. Shen, B. Pan, X. Zhang, K. Ikeuchi, K. Iida, A. Christianson, H. Walker, D. Adroja, M. Abdel-Hafiez, *et al.*, *Nature communications* **7**, 12182 (2016).
- ⁴² A. Shukla, M. Calandra, M. d'Astuto, M. Lazzeri, F. Mauri, C. Bellin, M. Krisch, J. Karpinski, S. M. Kazakov, J. Jun, D. Daghero, and K. Parlinski, *Phys. Rev. Lett.* **90**, 095506 (2003).
- ⁴³ V. Gnezdilov, Y. G. Pashkevich, P. Lemmens, D. Wulferding, T. Shevtsova, A. Gusev, D. Chareev, and A. Vasiliev, *Phys. Rev. B* **87**, 144508 (2013).
- ⁴⁴ R. Mittal, L. Pintschovius, D. Lamago, R. Heid, K.-P. Bohnen, D. Reznik, S. L. Chaplot, Y. Su, N. Kumar, S. K. Dhar, A. Thamizhavel, and T. Brueckel, *Phys. Rev. Lett.* **102**, 217001 (2009).
- ⁴⁵ V. Ksenofontov, G. Wortmann, A. I. Chumakov, T. Gasi, S. Medvedev, T. M. McQueen, R. J. Cava, and C. Felser, *Phys. Rev. B* **81**, 184510 (2010).
- ⁴⁶ M. Gang, Z. Xi-Yu, F. Lei, S. Lei, R. Cong, and W. Hai-Hu, *Chinese Physics Letters* **25**, 2221 (2008).
- ⁴⁷ J.-Y. Lin, Y. S. Hsieh, D. A. Chareev, A. N. Vasiliev, Y. Parsons, and H. D. Yang, *Phys. Rev. B* **84**, 220507 (2011).
- ⁴⁸ W. N. Lawless and A. J. Morrow, *Ferroelectrics* **15**, 159 (1977), <http://dx.doi.org/10.1080/00150197708237810>.
- ⁴⁹ R. O. Bell and G. Rupprecht, *Phys. Rev.* **129**, 90 (1963).
- ⁵⁰ G. Benedek, V. Celli, G. Comsa, R. Doak, J. Frenken, B. Hinch, H. Hoinkes, K. Kern, A. Lahee, J. Lapujoulade, *et al.*, *Helium atom scattering from surfaces*, Vol. 27 (Springer Science & Business Media, 2013).
- ⁵¹ D. Phelan, J. N. Millican, E. L. Thomas, J. B. Leão, Y. Qiu, and R. Paul, *Phys. Rev. B* **79**, 014519 (2009).
- ⁵² Y. Cao, S. Wang, S. Liu, Q. Guo, and J. Guo, *The Journal of Chemical Physics* **137**, 044701 (2012), <http://dx.doi.org/10.1063/1.4737946>.
- ⁵³ X. Zhu, Y. Cao, S. Zhang, X. Jia, Q. Guo, F. Yang, L. Zhu, J. Zhang, E. Plummer, and J. Guo, *Review of Scientific Instruments* **86**, 083902 (2015).
- ⁵⁴ D. Tabor, J. Wilson, and T. Bastow, *Surface Science* **26**, 471 (1971).
- ⁵⁵ E. R. Jones, J. T. McKinney, and M. B. Webb, *Phys. Rev.* **151**, 476 (1966).
- ⁵⁶ R. Reid, *physica status solidi (a)* **2**, K109 (1970).
- ⁵⁷ P. Debye, *Annalen der Physik* **348**, 49 (1913).
- ⁵⁸ I. Waller, *Zeitschrift für Physik* **17**, 398 (1923).
- ⁵⁹ R. James, *The Optical Principles of the Diffraction of X-rays*. (G. Bell and sons, 1952).
- ⁶⁰ N. W. Ashcroft and N. D. Mermin, *Solid state physics (holt, rinehart and winston, new york, 1976)* (1976) p. 793.
- ⁶¹ A. Togo and I. Tanaka, *Scripta Materialia* **108**, 1 (2015).
- ⁶² P. E. Blöchl, *Phys. Rev. B* **50**, 17953 (1994).
- ⁶³ G. Kresse and J. Furthmüller, *Phys. Rev. B* **54**, 11169 (1996).
- ⁶⁴ G. Kresse and D. Joubert, *Phys. Rev. B* **59**, 1758 (1999).
- ⁶⁵ P. Giannozzi, S. Baroni, N. Bonini, M. Calandra, R. Car, C. Cavazzoni, D. Ceresoli, G. L. Chiarotti, M. Cococcioni, I. Dabo, A. D. Corso, S. de Gironcoli, S. Fabris, G. Fratesi, R. Gebauer, U. Gerstmann, C. Gougousis, A. Kokalj, M. Lazzeri, L. Martin-Samos, N. Marzari, F. Mauri, R. Mazzarello, S. Paolini, A. Pasquarello, L. Paulatto, C. Sbraccia, S. Scandolo, G. Sclauzero, A. P. Seitsonen, A. Smogunov, P. Umari, and R. M. Wentzcovitch, *Journal of Physics: Condensed Matter* **21**, 395502 (2009).
- ⁶⁶ K. F. Garrity, J. W. Bennett, K. M. Rabe, and D. Vanderbilt, *Computational Materials Science* **81**, 446 (2014).
- ⁶⁷ J. P. Perdew, K. Burke, and M. Ernzerhof, *Phys. Rev. Lett.* **77**, 3865 (1996).
- ⁶⁸ H. Ibach and D. L. Mills, *Electron energy loss spectroscopy and surface vibrations* (Academic press, 1982).
- ⁶⁹ X. Zhu, L. Santos, R. Sankar, S. Chikara, C. . Howard, F. C. Chou, C. Chamon, and M. El-Batanouny, *Phys. Rev. Lett.* **107**, 186102 (2011).
- ⁷⁰ W. L. McMillan, *Phys. Rev.* **167**, 331 (1968).
- ⁷¹ L. Boeri, O. V. Dolgov, and A. A. Golubov, *Phys. Rev. Lett.* **101**, 026403 (2008).
- ⁷² T. Yildirim, O. Gülseren, J. W. Lynn, C. M. Brown, T. J. Udovic, Q. Huang, N. Rogado, K. A. Regan, M. A. Hayward, J. S. Slusky, T. He, M. K. Haas, P. Khalifah, K. Inumaru, and R. J. Cava, *Phys. Rev. Lett.* **87**, 037001 (2001).
- ⁷³ Y. Wang, L. Rademaker, E. Dagotto, and S. Johnston, *Phys. Rev. B* **96**, 054515 (2017).
- ⁷⁴ Y. Zhou and A. J. Millis, *Phys. Rev. B* **96**, 054516 (2017).
- ⁷⁵ R. Fuchs and K. L. Kliewer, *Phys. Rev.* **140**, A2076 (1965).